J|A|C|S
ARTICLES
Published on Web 03/01/2002

Oxalate-Bridged Complexes of Dimolybdenum and Ditungsten Supported by Pivalate Ligands: $(^tBuCO_2)_3M_2(\mu\text{-}O_2CCO_2)M_2(O_2C^tBu)_3$. Correlation of the Solid-State, Molecular, and Electronic Structures with Raman, Resonance Raman, and Electronic Spectral Data

Bruce E. Bursten,*,† Malcolm H. Chisholm,*,† Robin J. H. Clark,*,‡ Steven Firth,‡ Christopher M. Hadad,*,† Ann M. MacIntosh,§ Paul J. Wilson,† Patrick M. Woodward,*,† and Jeffrey M. Zaleski*,§

Contribution from the Department of Chemistry, The Ohio State University, 100 West 18th Avenue, Columbus, Ohio 43210, Christopher Ingold Laboratories, University College London, 20 Gordon Street, London WC1H 0AJ, U.K., and Department of Chemistry, Indiana University, 800 East Kirkwood Avenue, Bloomington, Indiana 47405

Received July 23, 2001. Revised Manuscript Received December 14, 2001

Abstract: The compounds $(^tBuCO_2)_3M_2(\mu\text{-}O_2CCO_2)M_2(O_2C^tBu)_3$ (M_4OXA), where M = Mo or W, are shown by analysis of powder X-ray diffraction data to have extended lattice structures wherein oxygen atoms from the oxalate and pivalate ligands of one M_4OXA molecule are linked to metal atoms of neighboring molecules. Raman, resonance Raman, electronic absorption (2−325 K in 2-MeTHF), and emission spectra are reported, together with corresponding spectra of the $\mu\text{-}O_2{}^{13}C{}^{13}CO_2$ isotopomers. To aid in the assignment, the Raman spectra of $K_2C_2O_4{\cdot}H_2O$ and $K_2{}^{13}C_2O_4{\cdot}H_2O$ have also been recorded. The visible region of the electronic spectra is dominated by intense, fully allowed MLCT transitions, M_2 δ to oxalate π^*, which show pronounced thermochromism and extensive vibronic progressions associated with the oxalate ligand at low temperatures. With excitation into these charge-transfer bands, strong resonance enhancement is seen for Raman bands assigned to the oxalate $\nu_1(a_g)$ and, to a lesser extent, $\nu_2(a_g)$ modes. Electronic structure calculations for the model compounds $(HCO_2)_3M_2(\mu\text{-}O_2CCO_2)M_2(O_2CH)_3$, employing density functional theory (gradient corrected and time-dependent) with the Gaussian 98 and ADF 2000 packages, predict the planar oxalate D_{2h} configuration to be favored, which maximizes M_2 δ to oxalate π^* back-bonding, and indicate low barriers (<8 kcal mol^{-1}) to rotation about the oxalate C−C bonds.

Introduction

Previously, we reported the initiation of a project aimed at the synthesis and characterization of one-dimensional polymers incorporating M−M multiple bonds.[1] In two limiting structural representations, we described these as perpendicular and parallel polymers, as shown in **I** and **II**, based on the alignment of the M−M axes with respect to the polymer propagation axis.

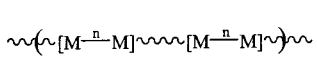

I

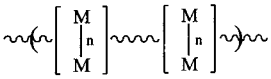

II

Given the diverse properties of compounds containing M−M bonds of order *n*, we anticipated that such metalloorganic polymers could contribute significantly to the development of materials chemistry based on inorganic−organic hybrids. Toward this end, a fuller understanding of the synthesis and bonding in $M_2{\cdots}M_2$ subunits is required, in addition to the synthesis, characterization, and manipulation of extended chains or oligomers.

We chose the compounds $M_2(O_2CR)_4$ (M = Mo or W) as the M_2 building blocks since their syntheses afforded access to significant quantities of materials, and their electronic structure had been studied extensively.[2] As a linker, we employed dicarboxylate ligands, $O_2C{-}X{-}CO_2$. However, problems with synthetic control over the products immediately arose, as the $M_2(O_2CR)_4$ compounds and their derivatives are kinetically labile. "Spontaneous self-assembly" does not yield a single product; rather mixtures of species are formed, none of which has been readily separable except for the "dimers of dimers", of formula $(^tBuCO_2)_3M_2(\mu\text{-}O_2C{-}X{-}CO_2)M_2(O_2C^tBu)_3$, which sometimes precipitate from toluene solution. Even these compounds have defied structural characterization by single-crystal

* To whom correspondence should be addressed. E-mail: bursten@chemistry.ohio-state.edu; chisholm@chemistry.ohio-state.edu; r.j.h.clark@ucl.ac.uk; hadad@chemistry.ohio-state.edu; woodward@chemistry.ohio-state.edu; zaleski@indiana.edu.
† The Ohio State University.
‡ University College London.
§ Indiana University.

(1) Cayton, R. H.; Chisholm, M. H.; Huffman, J. C.; Lobkovsky, E. B. *J. Am. Chem. Soc.* **1991**, *113*, 8709−8724.
(2) Cotton, F. A., Walton, R. A. *Multiple Bonds Between Metal Atoms*, 2nd ed.; Oxford University Press: Oxford, UK, 1993.

10.1021/ja011786j CCC: $22.00

X-ray crystallography, as suitable crystals have not been obtained. This is not an uncommon problem in the field of molecular solids built upon covalent networks whose structures involve the ordering and connecting of well-defined substructures.[3] However, the groups of Cotton,[4−6] Walton,[7] and Bonar-Law[8−10] have recently reported the synthesis and molecular structures of a wide variety of dicarboxylate-linked M_2-containing compounds with different supporting ligands.

$M_2(O_2CR)_4$ compounds typically form laddered or staircase structures in the solid state, as represented by **III**. Despite this common structural motif, there are numerous possible three-dimensional arrangements for these chains, and indeed, solid $Mo_2(O_2C^tBu)_4$ exists in three crystalline polymorphs.[11,12]

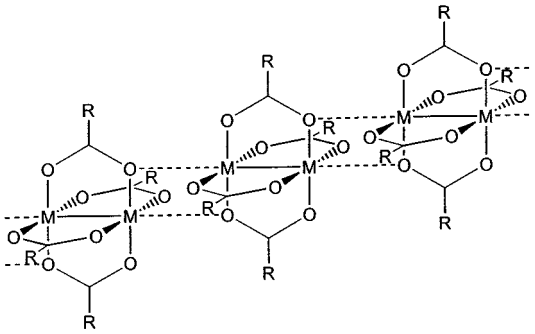

III

The properties of any "material" based on a $[M_2]_n(\text{bridge})_{n-1}$ chain will be dependent upon the nature of the intra- and interchain interactions in the solid state, whereas in solution, the molecular properties of a $[M_2]_n(\text{bridge})_{n-1}$ chain will be influenced by its interactions with the solvent and other molecules present in solution, including itself.

In this paper we describe our studies on the oxalate-bridged "dimers of dimers", $(^tBuCO_2)_3M_2(\mu\text{-}O_2CCO_2)M_2(O_2C^tBu)_3$ (M_4OXA), and show how these studies may be relevant to the design and construction of molecular devices based[13] on complexes that contain M_2 units with quadruple bonds.[2]

Results and Discussion

Solid-State Structures. Knowledge of solid-state and molecular structure is an obvious starting point upon which to base explanations of spectroscopic properties and an understanding of electronic structure. When routine attempts to obtain crystals of the M_4OXA compounds suitable for single-crystal X-ray diffraction studies failed, we resorted to determine the molecular packing in the solid-state and molecular conformation by alternate means, namely by a combination of solid-state NMR spectroscopy, powder X-ray diffraction, and electronic structure calculations.

^{13}C CPMAS NMR spectra of both the (μ-O_2CCO_2) and (μ-$O_2{}^{13}C{}^{13}CO_2$) isotopomers of Mo_4OXA showed a single oxalate carbon resonance, suggesting that we were indeed dealing with single-phase samples and that it was likely that all of the Mo_4-OXA molecules were crystallographically equivalent. Unfortunately, further details of the NMR spectra are difficult to interpret due to overlapping and coincidental resonances for the pivalate groups (see Experimental Section).

X-ray data were obtained from various samples of both Mo_4-OXA and W_4OXA sealed in glass capillaries both from the X7A beamline at the National Synchrotron Light Source at Brookhaven National Laboratory and from in-house monochromatic X-rays using a Bruker D8 diffractometer, equipped with an incident beam monochromator. Qualitatively, all of the data appeared to confirm that we were examining single-phase samples. The diffraction pattern of W_4OXA exhibited peak positions very similar to those of Mo_4OXA, clearly indicating that the two compounds are isostructural. Unfortunately, the W_4OXA peaks broadened more rapidly as a function of 2θ, and consequently were not suitable for detailed analysis.

The positions were determined using the peak fitting routine in DASH[14,15] and then put into the autoindexing program DICVOL-91.[16] For reasons which are fully explained in the Supporting Information, the preferred solution has space group symmetry *Pc* and unit cell dimensions $a = 16.054(2)$ Å, $b = 5.8170(6)$ Å, $c = 26.817(2)$ Å, and $\beta = 118.826(7)°$. Peak intensities were extracted with DASH for each of the unit cells using a whole pattern approach based on the Pawley method.[17]

We continued the structure solution by constructing a model with the correct intramolecular connectivity and reasonable bond distances. Our model was derived from the optimized gas-phase geometry of the model compound $(HCO_2)_3Mo_2(\mu\text{-}O_2CCO_2)$-$Mo_2(HCO_2)_3$, determined by density functional theory employing the Gaussian 98 package (see later), and replacing the formate protons by *tert*-butyl groups. The structure determination then proceeded by means of the global optimization approach implemented within DASH. Three variables were needed to describe the location of the molecule, four variables (quaternians[18]) to describe its orientation, six torsional degrees of freedom associated with the *tert*-butyl groups, and one torsional degree of freedom associated with the C−C bond of the oxalate group. Taken together, there are 14 parameters that can be varied during the simulated annealing process, a considerable reduction from the 156 structural variables associated with an unconstrained Rietveld refinement. Default simulated annealing parameters were used, and each trial solution was allowed to optimize using a process of rigid body Rietveld refinement.

The final fit to the experimental diffraction pattern is shown in Figure 1, and the final crystallographic parameters are tabulated and summarized in Tables 3 and 4 in the Supporting

(3) Yaghi, O. M.; Li, H.; Davis, C.; Richardson, D.; Groy, T. L. *Acc. Chem. Res.* **1998**, *31*, 474−484.
(4) Cotton, F. A.; Lin, C.; Murillo, C. A. *J. Chem. Soc., Dalton Trans.* **1998**, 3151−3154.
(5) Cotton, F. A.; Donahue, J. P.; Lin, C.; Murillo, C. A. *Inorg. Chem.* **2001**, *40*, 1234−1244.
(6) Cotton, F. A.; Lin, C.; Murillo, C. A. *Acc. Chem. Res.* **2001**, *34*, 759−771.
(7) Bera, J. K.; Angaridis, P.; Cotton, F. A.; Petrukhina, M. A.; Fanwick, P. E.; Walton, R. A. *J. Am. Chem. Soc.* **2001**, *123*, 1515−1516.
(8) Bonar-Law, R. P.; McGrath, T. D.; Singh, N.; Bickley, J. F.; Steiner, A. *Chem. Commun. (Cambridge)* **1999**, 2457−2458.
(9) Bickley, J. F.; Bonar-Law, R. P.; Femoni, C.; MacLean, E. J.; Steiner, A.; Teat, S. J. *Dalton* **2000**, 4025−4027.
(10) Bonar-Law, R. P.; Bickley, J. F.; Femoni, C.; Steiner, A. *Dalton* **2000**, 4244−4246.
(11) Cotton, F. A.; Extine, M.; Gage, L. D. *Inorg. Chem.* **1978**, *17*, 172−176.
(12) Martin, D. S.; Huang, H. W. *Inorg. Chem.* **1990**, *29*, 3674−3680.
(13) *Acc. Chem. Res.* **2001**, *34*, Issue 6, Molecular Machines Special Issue.
(14) DASH was written by W. I. F. David and K. Shankland and can be purchased from the Cambridge Crystallographic Data Centre; see www.ccdc.cam.ac.uk for more details.
(15) David, W. I. F.; Shankland, K.; Shankland, N. *Chem. Commun. (Cambridge)* **1998**, 931−932.
(16) Boultif, A.; Louer, D. *J. Appl. Crystallogr.* **1991**, *24*, 987−993.
(17) Pawley, G. S. *J. Appl. Crystallogr.* **1981**, *14*, 357−361.
(18) Leach, A. R., Ed. *Molecular Modeling: Principles and Applications*; Addison Wesley Longman Ltd.: Reading, MA, 1996.

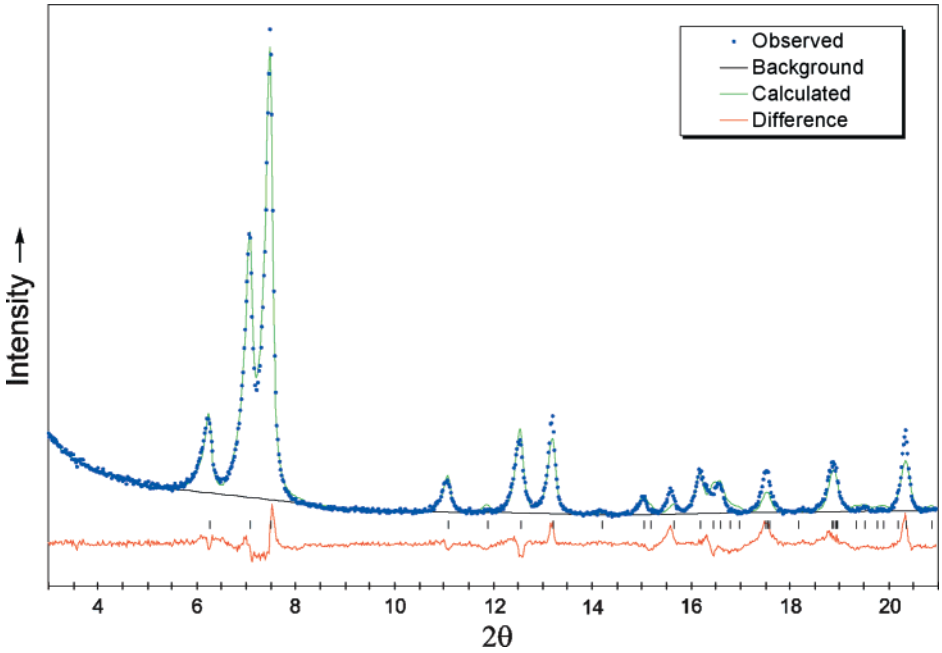

Figure 1. X-ray powder diffraction patterns for Mo_4OXA. The crosses represent the observed data points, while the solid line is the calculated fit to the diffraction pattern. The vertical lines at the bottom of the figure denote the expected peak positions.

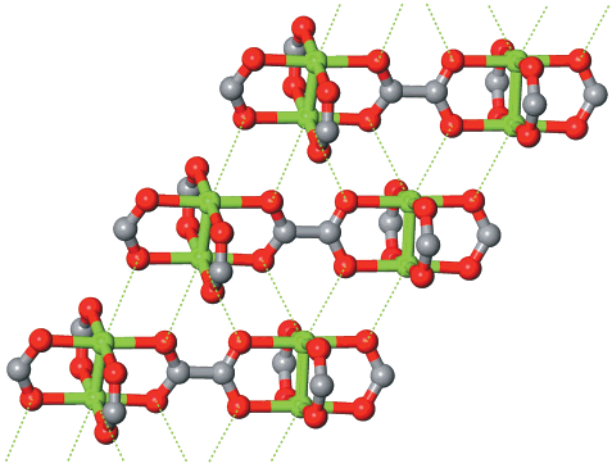

Figure 2. Intermolecular Mo−O interactions in Mo_4OXA which run parallel to the *b*-axis. All intermolecular Mo−O distances are 2.9(1) Å. The *tert*-butyl groups have been omitted for clarity, and the color scheme is Mo = green, O = red, and C = gray.

Information. Due to the large number of atoms contained in the unit cell and the relatively small number of observed independent reflections, all attempts to carry through with an unconstrained Rietveld refinement failed to provide further details of the structure.

The space-filling depictions (Figure 6 in the Supporting Information) illustrate the relatively high packing efficiency of these irregularly shaped molecules and the lack of overlap between *tert*-butyl groups on neighboring molecules. It should be emphasized that no constraints were used during the structure determination to prevent unwanted intermolecular overlap. Whereas the intermolecular interactions in the *ac* plane involve only weak van der Waals forces, Figure 2 shows that each Mo_4-OXA molecule is linked to its neighbors along the *b*-axis through four oxalate and two pivalate molybdenum-to-oxygen bonds each of 2.9−3.1(1) Å on either side of the molecule. The central $Mo_2O_2CCO_2Mo_2$ unit is not planar, but the oxalate torsion angle can reliably be estimated to fall between 15 and 20°, as described in detail in the Supporting Information.

There are certain structural features of this coordination polymer that clearly resemble the infinite ladder structure seen for the parent compound, $Mo_2(O_2C^tBu)_4$, as represented by **III**. However, in the present structure, the "side-on" chelating ability of the oxalate group is fully utilized, as evidenced by the five-membered rings to each Mo_2 unit within the Mo_4OXA molecule and the five-membered rings to the metal atoms of neighboring molecules.

While we are confident that the present solution unequivocally defines the coordination features of the solid-state and molecular structure of Mo_4OXA, we also recognize that the input model based on the calculated formate model gas-phase structure has not been significantly refined. As such, the Mo−Mo, Mo−O distances and their attendant angles are not precise in the way that a single-crystal X-ray diffraction solution would reveal. For example, an oxygen atom involved in an intermolecular Mo···O interaction would be expected to have a slightly larger intramolecular Mo−O distance by ca. 0.05 Å over one not so involved.[11,12] In our study, this distinction could not be made.

Bonding and Electronic Structure Calculations. When two M−M quadruple bonds are linked by a bridging oxalate ligand, the primary interactions between the metals and the dicarboxylate unit (aside from the formation of the M−O σ bonds) involve the filled δ orbitals of the metals and two of the oxalate π orbitals. There is a filled−filled interaction between the M_2 δ orbitals and one of the filled CO_2 π orbitals, shown in **IV**, and another involving donation from the M_2 δ orbital combination of opposite phase to one of the empty CO_2 π^* orbitals of oxalate, shown in **V**.

It is, however, important to note that there is little conformational preference in the oxalate dianion. AM1 and ab initio calculations indicate a slight preference for the 90° twisted D_{2d}

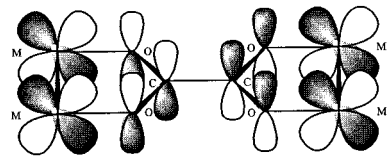

IV

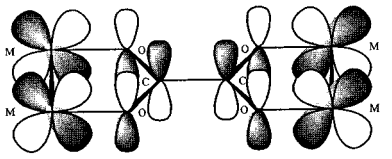

V

structure over the planar D_{2h} structure, $\Delta E \approx 5$ kcal mol^{-1}.[19] The Raman spectra of the oxalate anion in water indicate the D_{2d} rather than the D_{2h} structure to be favored, but in solid-state structures of the type $[Cr(C_2O_4)_3]^{3-}$ the oxalate ions bind to the metal ions, forming five-membered rings of the type shown in **VI**, where the planar or near-planar form of the anion is commonly seen.

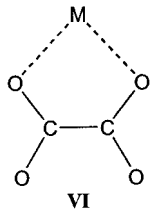

VI

The electronic coupling of the M_2 units is very sensitive to the oxalate C−C twist angle, θ. For $\theta = 0°$, the D_{2h} structure, the orbital interaction shown in **V** is maximized, but for $\theta = 90°$ it is at a minimum. Thus, rotation about the oxalate C−C bond will act like the rotation of a "dimmer-switch" with respect to $M_2\cdots M_2$ interactions through the oxalate π system.

To probe these interactions in a more quantitative manner, we have carried out molecular and electronic structure calculations using density functional theory (DFT) on the model compounds $(HCO_2)_3M_2(\mu\text{-}O_2CCO_2)M_2(O_2CH)_3$, where M = Mo or W, using both the Gaussian 98[20] and ADF 2000.01[21−24] programs (see Experimental Section for details).

Starting geometries for the formate model were built by utilizing literature values from $M_2(O_2CR)_4$ complexes[25−29] and estimating the oxalate C−C bond lengths to be 1.50 Å. Initial calculations were performed under D_2 symmetry with an initial oxalate C−C torsion angle of 45°. Optimization for both M = Mo and W led to pseudo D_{2h} geometries, implying such structures to be of lowest energy. Geometry optimization was repeated under strict D_{2h} symmetry (planar oxalate) for both M = Mo and W in order to simplify the bonding and orbital representations. The determined structures are illustrated in Figure 3, and selected geometric data are given in Table 1 for both M = Mo and W, from the Gaussian and ADF calculations, respectively. The geometrical parameters of the central $Mo_2O_2CCO_2Mo_2$ unit are similar to those in the solid-state structure of a (formamidinate)$_3$Mo$_2$(μ-O$_2$CCO$_2$)Mo$_2$(formamidinate)$_3$ complex.[4]

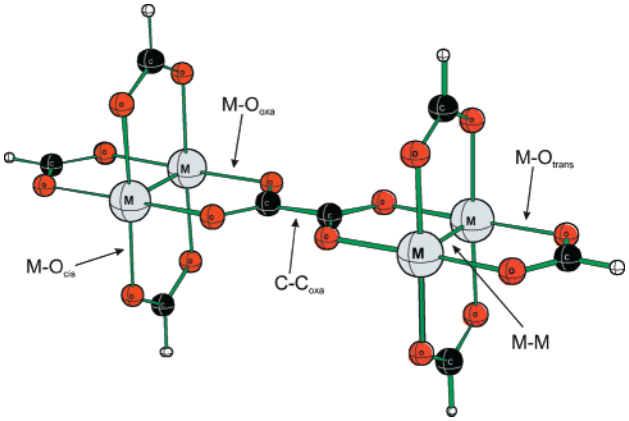

Figure 3. View of the fully relaxed D_{2h} $(HCO_2)_3M_2(\mu\text{-}O_2CCO_2)M_2(O_2CH)_3$, where M = Mo or W. Corresponding selected metrical data are given in Table 1.

Table 1. Calculated Geometric Data for the D_{2h} and D_{2d} Forms of the Formate Models of M_4OXA from Gaussian and ADF (in Parentheses) Calculations, Respectively

	MoD_{2h}/Å	MoD_{2d}/Å	WD_{2h}/Å	WD_{2d}/Å
M−M	2.122 (2.158)	2.119 (2.159)	2.205 (2.202)	2.202 (2.198)
M−O$_{oxa}$	2.097 (2.076)	2.127 (2.113)	2.072 (2.041)	2.113 (2.085)
M−O$_{trans}$	2.123 (2.115)	2.117 (2.103)	2.120 (2.107)	2.107 (2.093)
M−O$_{cis}$	2.121 (2.107)	2.119 (2.101)	2.112 (2.088)	2.101 (2.084)
C−C$_{oxa}$	1.503 (1.488)	1.516 (1.510)	1.477 (1.459)	1.509 (1.500)

It seemed clear that a planar $M_2O_2CCO_2M_2$ unit would be favored by the M_2-to-oxalate back-bonding shown in **V**, but in order to evaluate the true importance of this interaction, the C−C torsional angles, θ, were twisted to 90° and the structures reoptimized under D_{2d} symmetry. Selected geometric data for the D_{2d} structures are also given in Table 1. For both Mo and W, the differences between the calculated energies of the D_{2d} and the preferred D_{2h} structures are small; M = Mo, 3.0 and 4.4 kcal mol^{-1}, and M = W, 5.8 and 7.7 kcal mol^{-1}, from Gaussian and ADF determinations, respectively. These energy differences may be taken as estimates for the energy barriers to rotation about the oxalate C−C bonds.

The calculated orbital energies for the frontier MOs of the planar D_{2h} models are compared in Figure S2 of the Supporting Information. For both Mo and W, the HOMO and HOMO−1 are found to be the in- and out-of-phase M_2 δ orbital combina-

(19) Dewar, M. J. S.; Zheng, Y. J. *THEOCHEM* **1990**, *68*, 157−162.
(20) Frisch, M. J.; Trucks, G. W.; Schlegel, H. B.; Scuseria, G. E.; Robb, M. A.; Cheeseman, J. R.; Zakrzewski, V. G.; Montgomery, J. A., Jr.; Stratmann, R. E.; Burant, J. C.; Dapprich, S.; Millam, J. M.; Daniels, A. D.; Kudin, K. N.; Strain, M. C.; Farkas, O.; Tomasi, J.; Barone, V.; Cossi, M.; Cammi, R.; Mennucci, B.; Pomelli, C.; Adamo, C.; Clifford, S.; Ochterski, J.; Petersson, G. A.; Ayala, P. Y.; Cui, Q.; Morokuma, K.; Malick, D. K.; Rabuck, A. D.; Raghavachari, K.; Foresman, J. B.; Cioslowski, J.; Ortiz, J. V.; Stefanov, B. B.; Liu, G.; Liashenko, A.; Piskorz, P.; Komaromi, I.; Gomperts, R.; Martin, R. L.; Fox, D. J.; Keith, T.; Al-Laham, M. A.; Peng, C. Y.; Nanayakkara, A.; Gonzalez, C.; Challacombe, M.; Gill, P. M. W.; Johnson, B. G.; Chen, W.; Wong, M. W.; Andres, J. L.; Head-Gordon, M.; Replogle, E. S.; Pople, J. A. *Gaussian 98*, revision A9; Gaussian, Inc.: Pittsburgh, PA, 1998.
(21) Baerends, E. J.; Ellis, D. E.; Ros, P. *Chem. Phys.* **1973**, *2*, 41−51.
(22) Versluis, L.; Ziegler, T. *J. Chem. Phys.* **1988**, *88*, 322−328.
(23) te Velde, G.; Baerends, E. J. *J. Comput. Phys.* **1992**, *99*, 84−98.
(24) Guerra, C. F.; Snijders, J. G.; te Velde, G.; Baerends, E. J. *Theor. Chem. Acc.* **1998**, *99*, 391−403.
(25) Cotton, F. A.; Norman, J. G., Jr. *J. Coord. Chem.* **1972**, *1*, 161−171.
(26) Cotton, F. A.; Mester, Z. C.; Webb, T. R. *Acta Crystallogr., Sect. B* **1974**, *B30*, 2768−2770.
(27) Garner, C. D.; Hillier, I. H.; Walton, I. B.; Beagley, B. *J. Chem. Soc., Dalton Trans.* **1979**, 1279−1282.
(28) Santure, D. J.; McLaughlin, K. W.; Huffman, J. C.; Sattelberger, A. P. *Inorg. Chem.* **1983**, *22*, 1877−1883.
(29) Santure, D. J.; Huffman, J. C.; Sattelberger, A. P. *Inorg. Chem.* **1985**, *24*, 371−378.

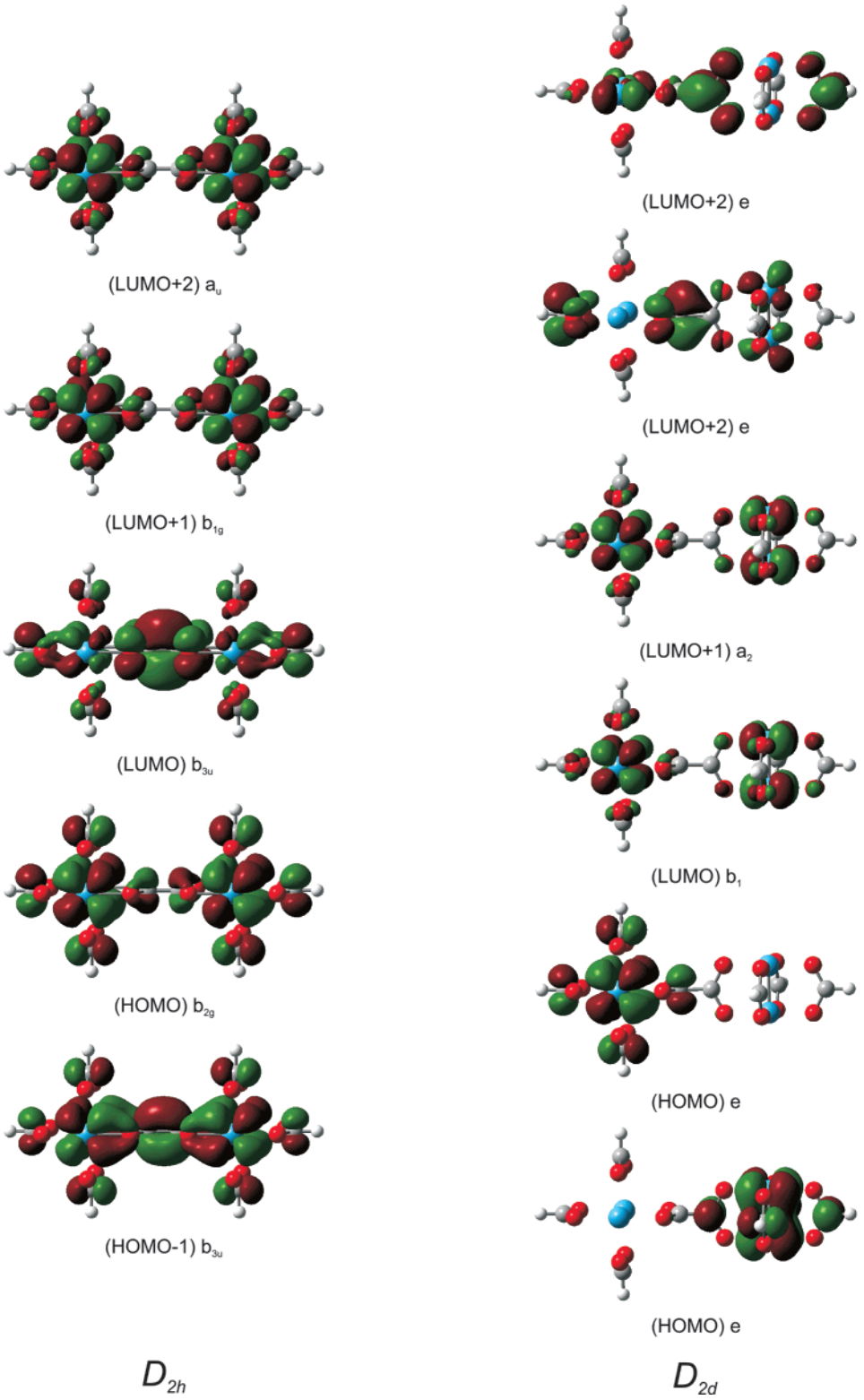

Figure 4. Molecular orbital plots for the frontier molecular orbitals of both D_{2h} and D_{2d} $(HCO_2)_3W_2(\mu\text{-}O_2CCO_2)W_2(O_2CH)_3$.

tions that interact with the oxalate π orbitals, as illustrated by **IV** and **V**. The splitting between these metal-based orbitals is calculated to be 0.40 eV for M = Mo and 0.59 eV for M = W (ADF). The larger splitting for tungsten arises because the W_2 δ orbitals are higher in energy than the Mo_2 δ orbitals and are therefore closer in energy to the lowest vacant oxalate-based b_{3u} orbital. This explains why the optimized C−C bond lengths are slightly shorter in the case of the tungsten complex and also, in part, why the calculated energy differences between the planar (D_{2h}) and the twisted (D_{2d}) structures are greater for tungsten than for molybdenum.

The calculated orbital energies of the b_{2g} HOMOs are −5.03 and −4.55 eV for M = Mo and W, respectively (ADF). These calculations imply that the W_4OXA compound should be the more easily oxidized, and, indeed, this correlates well with the observed electrochemical data obtained from cyclic voltamme-

Table 2. Comparison of the Calculated Lowest δ-to-Oxalate Transition Energies Determined by TDDFT for the Formate Models of M_4OXA by Gaussian and ADF (in Parentheses), and the Experimentally Observed Values for M_4OXA in THF Solution at Room Temperature

	calcd excitation wavelength/nm	calcd excitation energy/eV	calcd oscillator strength (f)	obsd λ_{max} THF/nm	obsd energy THF/eV	obsd ϵ THF/M^{-1} cm^{-1}
MoD_{2h}	449 (515)	2.76 (2.41)	0.515 (0.539)	460	2.70	14 200
MoD_{2d}	307 (353)	4.03 (3.51)	0.293 (0.343)			
WD_{2h}	529 (573)	2.34 (2.17)	0.723 (0.735)	704	1.76	36 400
WD_{2d}	363 (399)	3.42 (3.11)	0.310 (0.349)			

try, where the first oxidation for W_4OXA is found at a potential ca. 0.5 V lower than for $W_2(O_2C^tBu)_4$ and ca. 1.0 V lower than for Mo_4OXA.[1]

For the molybdenum model compound, the LUMO and LUMO+1 are M_2 δ* orbitals which are calculated to lie just lower in energy than the b_{3u} lowest unoccupied oxalate-based π orbital, whereas for the tungsten model compound, the LUMO is the b_{3u} lowest unoccupied oxalate-based π orbital, the counterpart to the stabilized δ combination of the same symmetry. The HOMO−LUMO gaps are calculated to be 1.94 and 1.55 eV for molybdenum and tungsten, respectively (ADF). The frontier molecular orbitals for the tungsten model compound are shown in Figure 4.

From the electronic structures of the planar D_{2h} oxalate-bridged structures, it is evident that the electronic spectra of the M_4OXA compounds will be dominated by the fully allowed MLCT $^1b_{2g} \rightarrow {}^1b_{3u}$ transition. In the case of M = Mo, the δ-to-δ* metal-based transitions which are allowed by symmetry will be much too weak to be seen due to their close proximity to this MLCT band. In THF solution, Mo_4OXA shows a broad intense absorption at $\lambda_{max} \approx 460$ nm, $\epsilon \approx 14\,200$ M^{-1} cm^{-1} and for W_4OXA $\lambda_{max} \approx 704$ nm, $\epsilon \approx 36\,400$ M^{-1} cm^{-1}. More details of the electronic spectra of the M_4OXA species are reported later in this article, but at this point it is worth noting that the calculations support these original spectral assignments and readily account for the significant red shift of the W_4OXA spectra and their higher molar absorptivities in relation to those of Mo_4OXA.[1]

To gain more insight into the nature of the observed electronic spectral features and also as an aid to determining the solution structure of the M_4OXA species, we have used the rapidly emerging time-dependent density functional theory (TDDFT) in calculating the vertical transition energies for $(HCO_2)_3M_2(\mu\text{-}O_2CCO_2)M_2(O_2CH)_3$.[30−34] Electronic transition energies for the lowest MLCT δ-to-oxalate transition are listed in Table 2 for calculations performed on the D_{2h} planar structure and the D_{2d} twisted structure, using both Gaussian 98 and ADF 2000, along with the λ_{max} data observed for the M_4OXA complexes in THF solution at room temperature.[1]

The calculated excitation energies for the lowest MLCT δ-to-oxalate transitions clearly show a significant dependence upon the oxalate C−C torsional angle, with the lower angle corresponding to the lower energy transition. In the twisted, $\theta = 90°$, D_{2d} structure the conjugation of the oxalate π orbitals is almost completely removed (see Figure 4), the lowest energy oxalate CO_2 π* orbital is now close in energy to the CO_2 π* orbitals of the formate, and the LUMO and LUMO+1 are the M_2 δ* combinations. Thus, the lowest MLCT-to-oxalate transition is observed at higher energy than in the D_{2h} equivalents. Under general D_2 symmetry, we can construct an energy correlation diagram connecting the two limiting D_{2h} and D_{2d} structural forms of the molecules. Based on the calculations for the formate models, we arrive at the frontier orbital energy correlation diagram shown in Figure 5, which clearly shows how the "equivalent" frontier orbitals rearrange as the oxalate C−C torsional angle is changed.

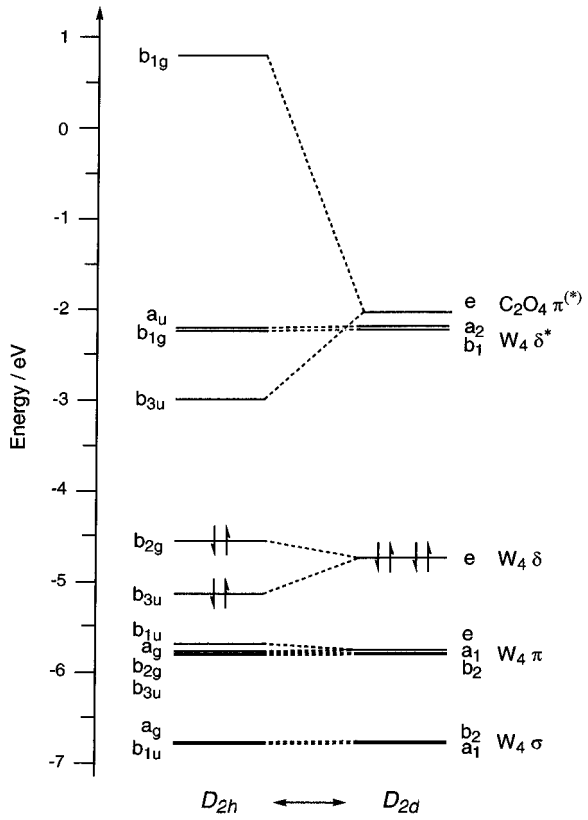

Figure 5. Comparative molecular orbital energy level diagram for D_{2h} and D_{2d} $(HCO_2)_3W_2(\mu\text{-}O_2CCO_2)W_2(O_2CH)_3$.

The TDDFT results for the molybdenum complex reproduce the magnitude of the transition energy exceptionally well and appear to imply that, in solution, a geometry close to the limiting D_{2h} structure exists for M_4OXA, with the disclaimers that the calculations are performed in the gas phase and in the absence of the effects of coordinating solvents, and give vertical excitations from only one conformer, whereas the experimental results are adiabatic and could arise from conformations that exist as a Boltzmann average under the experimental conditions. The equivalent predicted transition energies for the tungsten model compound show an identical trend, although the experi-

(30) Gross, E. K. U.; Kohn, W. *Adv. Quantum Chem.* **1990**, *21*, 255−291.
(31) Bauernschmitt, R.; Ahlrichs, R. *Chem. Phys. Lett.* **1996**, *256*, 454−464.
(32) Stratmann, R. E.; Scuseria, G. E.; Frisch, M. J. *J. Chem. Phys.* **1998**, *109*, 8218−8224.
(33) van Gisbergen, S. J. A.; Snijders, J. G.; Baerends, E. J. *Comput. Phys. Commun.* **1999**, *118*, 119−138.
(34) Rosa, A.; Baerends, E. J.; van Gisbergen, S. J. A.; Lenthe, E. v.; Groeneveld, J. A.; Snijders, J. G. *J. Am. Chem. Soc.* **1999**, *121*, 10356−10365.

Table 3. Wavenumbers and Assignments for the Raman Bands of $Mo_2(O_2C^tBu)_4$ and $W_2(O_2C^tBu)_4$ with 514.5 nm Excitation[a]

$Mo_2(O_2C^tBu)_4$ ν/cm^{-1}	$W_2(O_2C^tBu)_4$ ν/cm^{-1}	assignment	$Mo_2(O_2C^tBu)_4$ ν/cm^{-1}	$W_2(O_2C^tBu)_4$ ν/cm^{-1}	assignment
306w		ν(MoO)	1366vw	1360s	$\delta_s(CH_3)$
332vw	340w	ν(MO)	1383s	1367s, sh	$\delta_s(CH_3)$
403s	318s	ν(MM)		1372vs	$\delta_s(CH_3)$
420vw	430w	$\rho(CO_2)$	1416m	1406s	$\nu_s(CO_2)$
439w	447m	$\rho(CO_2)$	1426s	1413s	$\nu_s(CO_2)$
450w	455m	$\rho(CO_2)$		1428w	
607vw	619m, sh		1439w	1437w	$\delta_{as}(CH_3)$
624m	626s	$\delta(CO_2)$	1458m	1454w	$\delta_{as}(CH_3)$
632m	635s	$\delta(CO_2)$	1483m	1476w	$\delta_{as}(CH_3)$
	753w	ν(WW) + $\rho(CO_2)$	1490w	1485w	$\delta_{as}(CH_3)$
	759w	ν(WW) + $\rho(CO_2)$		1509w	
778w				1519w	
	802w			1528w	ν(WW) + $\nu(CMe_3)$
806s		2ν(MoMo)	1542w		
	807w		1552w		$\delta(CO_2) + \rho(CH_3)$
902m	900s	$\nu(CCMe_3)$		2730w	$\nu_s(CO_2) + \delta_s(CH_3)$
907w	905m	$\nu(CCMe_3)$		2774w	$\nu_s(CO_2) + \delta_s(CH_3)$
934w	933w	$\rho(CH_3)$		2867w	ν(CH)
938w	937w	$\rho(CH_3)$	2904w	2904w	ν(CH)
943w		$\rho(CH_3)$	2927m	2927m	ν(CH)
1210w		3ν(MoMo)	2965m	2964m	ν(CH)
1218w	1213m	ν(CMe)	2984w	2999w	ν(CH)
1231w	1224m	ν(CMe)	3009vw		ν(CH)

[a] $Mo_2(O_2C^tBu)_4$ as a 50% KCl disk and $W_2(O_2C^tBu)_4$ as the pure crystalline solid within a capillary, both at ca. 80 K.

mentally observed excitation energy is even lower in energy than that calculated for the D_{2h} structure. The absence of spin−orbit coupling considerations in our calculations (satisfactory convergence could not be achieved) would go some way to explaining the discrepancy for the tungsten species, whose orbitals would be considerably perturbed by such effects.

Raman and Resonance Raman Spectra. Since the M_4OXA compounds show intense electronic absorptions in the visible region assignable to M_2 δ-to-oxalate-based π transitions, it was expected that these compounds would show interesting Raman and resonance Raman spectra.

To determine typical $^{12}C/^{13}C$ shifts of the oxalate modes, the Raman spectra of $K_2{}^{12}C_2O_4{\cdot}H_2O$ and $K_2{}^{13}C_2O_4{\cdot}H_2O$ have each been recorded as pressed disks of the crystalline salt with ca. 100 mW of 514.5 nm radiation at ca. 80 K. The band wavenumbers of $K_2{}^{12}C_2O_4{\cdot}H_2O$ are virtually identical to those reported from a Raman study of a single crystal at room temperature.[35] The key assignments are for the a_g modes, ν_1 at 1445 cm^{-1} (^{13}C isotopic shift of 35 cm^{-1}), ν_2 at 879 cm^{-1} (^{13}C isotopic shift of 8 cm^{-1}), and ν_3 at 475 cm^{-1} (^{13}C isotopic shift of 1 cm^{-1}).

The three totally symmetric symmetry coordinates, S_1-S_3, of the oxalate dianion, represented in **VII** below, are often identified in the literature with the normal coordinates $\nu_s(CO_2)$, ν(CC), and $\delta_s(CO_2)$, respectively. However, extensive mixing of the symmetry coordinates in the normal modes does occur. Thus, in this paper we shall simply label the modes ν_1, ν_2, and ν_3 in order of decreasing wavenumber.

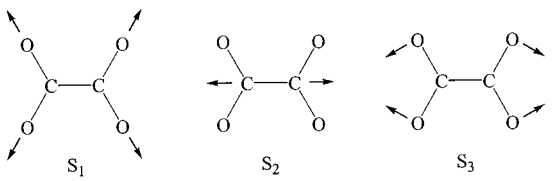

VII

(35) Erikson, A.; Nielsen, O. F. *J. Mol. Struct.* **1978**, *48*, 343.

Raman spectra of $Mo_2(O_2C^tBu)_4$ and $W_2(O_2C^tBu)_4$ were recorded using 45 and 11 mW, respectively, of 514.5 nm radiation and spectral slit widths of 2 cm^{-1}. The spectra are provided in Figure S3 in the Supporting Information, and the band wavenumbers are given in Table 3. The assignments are made by comparison with the Raman spectra of $Mo_2(O_2CCH_3)_4$,[36] $Mo_2(O_2CCD_3)_4$,[36] and $^tBuCO_2H$.[37] A spectrum of $Mo_2(O_2C^tBu)_4$ was also recorded using 15 mW of 457.9 nm radiation and a spectral slit width of 2 cm^{-1}. This wavelength lies within the envelope of the weak ($\epsilon \approx 100$ M^{-1} cm^{-1}) band of the Mo_2 δ-to-δ^* electronic transition; however, no changes in the relative intensities of the bands were detected.

Raman and Resonance Raman Spectra of Mo_4OXA. The Raman spectrum of Mo_4OXA was excited with ca. 100 mW of 647.1 nm radiation and recorded with a spectral slit width of 2 cm^{-1}. The spectrum is shown in Figure 6, and the observed bands and probable assignments are given in Table 4. The assignments are based in part on the Raman spectrum of $Mo_2(O_2C^tBu)_4$ as reported above and also on the vibrational spectra of a variety of metal oxalate complexes.[38] Of note is the fact that it is the oxalate-based bands which dominate the Raman spectra of Mo_4OXA, predominantly $\nu_1(a_g)$ at 1411 cm^{-1}, its first overtone at 2815 cm^{-1}, $\nu_2(a_g)$ at 932 cm^{-1}, and $\nu_3(a_g)$ at 576 cm^{-1}, along with ν(Mo−Mo) at 395 cm^{-1}. The assignments are confirmed by the $^{12}C/^{13}C$ isotopic shifts displayed by each mode in comparison with those displayed by $K_2C_2O_4{\cdot}H_2O$. Thus, the isotopic shifts of $\nu_1(a_g)$ and $2\nu_1(a_g)$ are 44 and 90 cm^{-1}, respectively, that of $\nu_2(a_g)$ is 4 cm^{-1}, that of $\nu_3(a_g)$ is 3 cm^{-1}, and that of ν(Mo−Mo) is ca. 0 cm^{-1}. The appearance of several overtone and combination bands involving $\nu_1(a_g)$ in the 647.1 nm Raman spectrum of Mo_4OXA implies that, even at this excitation wavelength, significant preresonance effects are operating.[39]

(36) Clark, R. J. H.; Hempleman, A. J.; Kurmoo, M. *J. Chem. Soc., Dalton Trans.* **1988**, 973−981.
(37) Longueville, W.; Fontaine, H. *J. Raman Spectrosc.* **1978**, *7*, 238−243.
(38) Fujita, J.; Martell, A. E.; Nakamoto, K. *J. Chem. Phys.* **1962**, *36*, 324.
(39) Clark, R. J. H.; Dines, T. J. *Angew. Chem.* **1986**, *98*, 131−160.

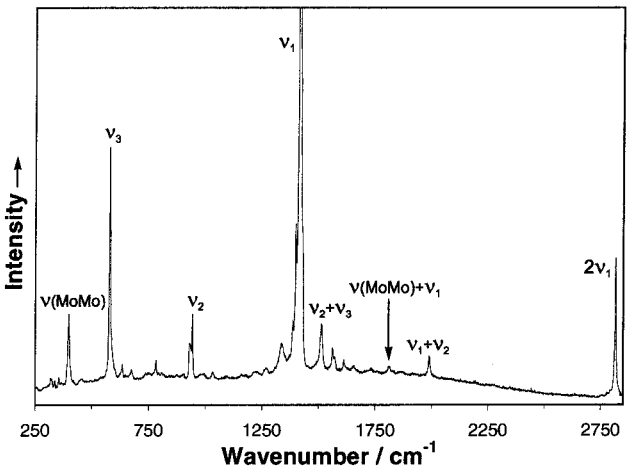

Figure 6. Raman spectrum of Mo_4OXA as a 50% KCl disk at ca. 80 K, with 100 mW of 647.1 nm excitation and a spectral slit width of 2 cm^{-1}.

Table 4. Wavenumbers and Assignments for the Raman Bands of Mo_4OXA and $Mo_4{}^{13}C$-OXA with 647.1 nm Excitation[a]

Mo_4OXA ν/cm^{-1}	$Mo_4{}^{13}C$-OXA ν/cm^{-1}	assignment
236w	231w	
317vw	316w	ν(MoO)
333vw		ν(MoO)
352vw		ν(MoO)
395m	396w	ν(MoMo)
576s	573m	ν_3
632w		$\delta_s(CO_2)$ (piv)
671w		$\delta_s(CO_2)$ (piv)
779w		ν(CC) (piv)
932m	928w	ν_2
940m		$\rho(CH_3)$
1031w		
1220w, br		$\nu(CCH_3)$
1265w	1257vw	
1334m	1329m	ν(MoMo) + ν_2
	1339s	
1383m		$\delta_s(CH_3)$
1395s	1392	$\delta_s(CH_3)$
1411vs	1367vs	ν_1
1425s, sh	1430vw	$\nu_s(CO_2)$ (piv)
	1461w	
1509m		$\nu_2 + \nu_3$
1559m		$\nu_a(CO_2)$ (ox)
1569w, sh		
1609w		$\delta_s(CO_2) + \rho(CH_3)$ (?)
1650vw		$\nu_s(CO_2)$ + 236
1808vw		ν(MoMo) + ν_1
1987m	1937vw	$\nu_1 + \nu_2$
	2667vw	ν(MoMo) + ν_2 + 1339
2815s	2725m	$2\nu_1$

[a] As 50% KCl disks at ca. 80 K.

The Raman spectrum of Mo_4OXA at resonance with the ca. 480 nm band (assigned to a MLCT band, vide infra) has been obtained on a 1:1 disk of Mo_4OXA and K_2SO_4 at liquid nitrogen temperature with 30 mW of 488.0 nm radiation (Figure 7), the band maxima being assigned in Table 5. The relative intensities have been measured as the areas of Lorentzian functions fitted to each band profile, after correcting the spectrum for the wavelength dependence of the spectrometer throughput and the ν^4 dependence of the scattered light intensity. Immediately apparent is the immense intensification at resonance of the band attributed to $\nu_1(a_g)$ of the oxalate ligand and to those attributed to its combination bands with other totally symmetric modes

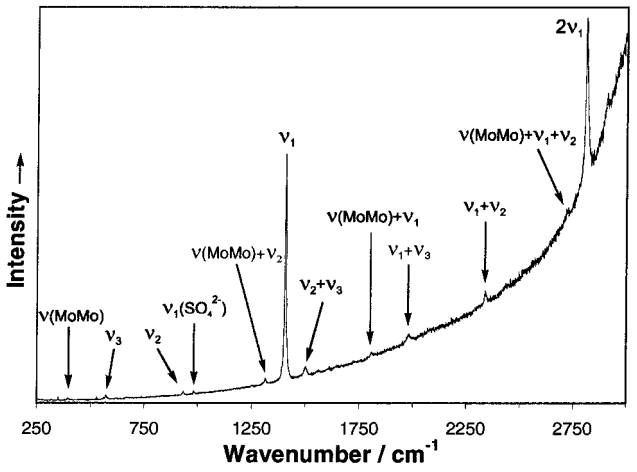

Figure 7. Resonance Raman spectrum of Mo_4OXA as a 50% K_2SO_4 disk at ca. 80 K, with 488.0 nm excitation and a spectral slit width of 2 cm^{-1}.

Table 5. Wavenumbers, Assignments, and $^{12}C/^{13}C$ Isotopic Shifts for the Resonance Raman Bands of Mo_4OXA and $Mo_4{}^{13}C$-OXA with 488.0 nm Excitation[a]

Mo_4OXA		$Mo_4{}^{13}C$-OXA		isotopic shift Δ/	
ν/cm^{-1}	relative intensity	ν/cm^{-1}	relative intensity	cm^{-1}	assignment
395	1	396	2	+1	ν(MoMo)
576	2	572	3	−4	ν_3
932	2	925	6	−7	ν_2
		1272	8		
1314	2				ν(MoMo) + ν_2
1411	83	1366	82	−45	ν_1
		1460	3		
1500	8				$\nu_2 + \nu_3$
		1516	11		
1808	1	1762	<1	−46	ν(MoMo) + ν_1
1987	4	1939	10	−49	$\nu_1 + \nu_3$
2339	8	2287	6	−52	$\nu_1 + \nu_2$
2722	6				ν(MoMo) + $\nu_1 + \nu_2$
2815	100	2725	100	−90	$2\nu_1$

[a] As 50% K_2SO_4 disks at ca. 80 K.

of oxalate, $\nu_2(a_g)$ and $\nu_3(a_g)$, with ν(Mo−Mo), but not with any of the bands associated with the pivalate ligands.

Due to problems of sample homogeneity and decomposition in the K_2SO_4 disk, the $SO_4{}^{2-}$ $\nu_1(a_1)$ band could not be used as a reliable, internal intensity standard for determining the excitation profile of the 1411 cm^{-1} band. Instead, the ratio of the intensity of this band to that of the ν(Mo−Mo) band was plotted as a function of the excitation wavelength. Although this is not a completely satisfactory way of defining the excitation profile, due to possible changes in the relative intensity of the band attributed to ν(Mo−Mo), it can be seen that there is a reasonable correlation between this ratio and the electronic band profile in the 480 nm region (see Figure S4 in the Supporting Information.) In fact, the variation of the band intensity of ν(Mo−Mo) with wavelength is expected to be small (as also found for the intensity of the analogous band, ν(W−W), of W_4OXA, see later). Also shown in Figure S4 is the intensity of the overtone at 2815 cm^{-1} relative to that of the fundamental at 1411 cm^{-1}. It is often found that the relative intensity of an overtone peak increases rapidly at resonance, the excitation profile maximizing at about one quantum in the enhanced mode to higher wavenumber than does that of the fundamental,[39] as is seen here. Sample fluorescence precluded

Table 6. Wavenumbers and Assignments for the Raman Bands of W_4OXA and $W_4{}^{13}C$-OXA with 647.1, 568.2, and 514.5 nm Excitation[a]

647.1 nm ν/cm^{-1}		568.2 nm ν/cm^{-1}		514.5 nm ν/cm^{-1}		
^{12}C	^{13}C	^{12}C	^{13}C	^{12}C	^{13}C	assignment
311m	314m	311m	311m	311w	310w	ν(WW)
582m	585m	582w	584w	582m	582w	ν_3
606w		606vw				2ν(WW)
766vw	766w	766vw	766w	767vw	765w	ν(CCMe$_3$)
828vw	828w					
895m	897m	895w	898vw	897vw	896w	ν(WW) + ν_3
915s	916s	915s	916s	916s	914s	ν_2
1001w	1003w	1001vw				
		1162vw		1162vw		
1234m	1193m	1235m	1191m	1235m	1191m	ν(WW) + ν_2
	1228w					
1319s	1276s	1319s	1276s	1318s	1275s	ν_1
	1366m		1364w	1372w	1367w	
1407m		1407w		1408w		δ_s(CH$_3$)
				1435w		ν_s(CO$_2$) (piv)
1462vw	1422w	1462vw	1425w	1459w	1416w	ν_1 + 144
	1591vw		1587w		1586w	ν(WW) + ν_1
1828w	1828m	1828vw	1826w		1824vw	$2\nu_2$
					1860w	
				2133vw		
2236w	2193m	2236w	2191m	2234m	2187m	ν_1 + ν_2
2325vw						
		2554w	2468vw	2552vw	2464w	ν(WW) + ν_1 + ν_2
2638w	2559m	2638m	2553m	2638m	2548m	$2\nu_1$
				2855vw		ν(CH)
				3142vw		ν(CH)

[a] As the pure crystalline solids within capillaries at ca. 80 K.

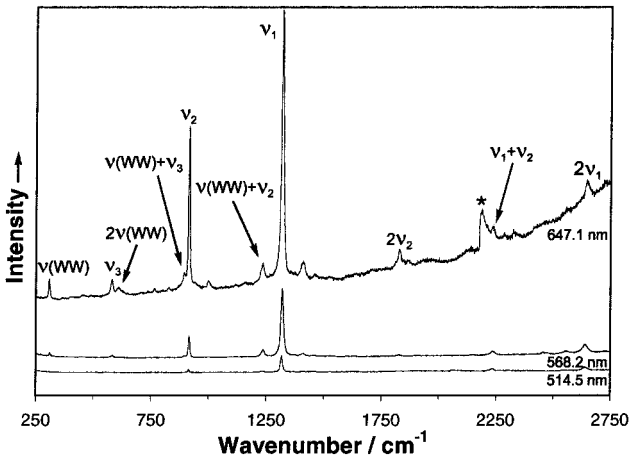

Figure 8. Resonance Raman spectra of W_4OXA as the pure crystalline solid within capillaries at ca. 80 K, with 647.1 (29 mW), 568.2 (37 mW), and 514.5 (41 mW) nm excitation and spectral slit widths of 2 cm^{-1}. Spectra are corrected for laser power, spectrometer throughput, and the ν^4 scattering efficiency. The feature marked with an asterisk is due to a sudden fluctuation in laser power.

the observation of harmonics of the 1411 cm^{-1} mode higher than the second.

Raman and Resonance Raman Spectra of W_4OXA. Spectra were recorded with 676.4, 647.1, 568.2, 514.5, 488.0, and 457.9 nm excitation, all with a 4 cm^{-1} spectral slit width. Spectra recorded with 676.4 and 457.9 nm excitation were very weak and of poor quality; that recorded with 488.0 nm excitation was also very weak, and only the strongest bands could be observed. The spectra obtained with 647.1, 568.2, and 514.5 nm excitation were resonance enhanced and are shown in Figure 8. In defining the oxalate-based spectral bands, the nomenclature ν_1, ν_2, and ν_3 has again been used in order of decreasing wavenumber. The band maxima in these spectra are listed in Table 6, along with probable assignments.

Due to the large amount of scatter from these samples, it was difficult to see any signals below ca. 300 cm^{-1}, and so no bands attributable to W−O stretches could be detected. The band at 311 cm^{-1} can confidently be assigned to ν(W−W); this is a typical value for quadruply bonded tungsten compounds.[2] The strongest band in the spectrum is at 1319 cm^{-1}, with its overtone appearing at 2638 cm^{-1}. This band is assigned to $\nu_1(a_g)$ of the oxalate group, analogous to the 1411 cm^{-1} band of Mo_4OXA. The assignments are confirmed by the $^{12}C/^{13}C$ isotopic shifts, which for $\nu_1(a_g)$ and $2\nu_1(a_g)$ are 43 and 85 cm^{-1}, respectively, but for $\nu_2(a_g)$, $\nu_3(a_g)$, and ν(W−W) are ca. 0 cm^{-1}.

Excitation profiles for the most resonance-enhanced bands of W_4OXA were derived from the band intensities after correcting the spectra as described for Mo_4OXA. As these samples were sealed in capillary tubes, there were no problems with decomposition or inhomogeneity, so the corrected intensities were plotted directly against excitation line wavelength, i.e., without the use of an internal standard. The excitation profiles (Figure S5 in the Supporting Information) show a good correspondence with the envelope of the electronic band. As in the case of Mo_4OXA, $\nu_1(a_g)$ is greatly enhanced at resonance with the W−W δ-to-oxalate π^* transition as is its first overtone, as well as—but to a much lesser extent—its combination bands with the other totally symmetric modes ν(W−W), $\nu_2(a_g)$, and $\nu_3(a_g)$, but not with any of the pivalate modes. It is noteworthy that the $\nu_2(a_g)$ band is much more enhanced for the tungsten than for the analogous molybdenum complex.

A summary of the selected Raman data is given in Table 7, thereby allowing a ready comparison of oxalate a_g and ν(M−M) modes for the complexes studied. On ^{13}C-for-^{12}C substitution of the oxalate carbon atoms, $\nu_1(a_g)$ is reduced by ca. 40 cm^{-1}, whereas the other a_g modes are affected to much lesser extents (ca. 4 cm^{-1}). That $\nu_1(a_g)$ is lower for the M_4OXA complexes than for $K_2C_2O_4{\cdot}H_2O$ may be due in part to the relative masses

Table 7. Summary of the Wavenumbers for the Key Raman Bands of the $^{12}C/^{13}C$ Isotopomers of $K_2C_2O_4$, Mo_4OXA, and W_4OXA

band	$K_2{}^{12}C_2O_4$ ν/cm^{-1}	$K_2{}^{13}C_2O_4$ ν/cm^{-1}	Mo_4OXA ν/cm^{-1}	$Mo_4{}^{13}C$-OXA ν/cm^{-1}	W_4OXA ν/cm^{-1}	$W_4{}^{13}C$-OXA ν/cm^{-1}
ν_1	1445	1410	1411	1367	1319	1276
ν_2	879	870	932	927	915	915
ν_3	475	474	576	573	582	584
ν(MM)			395	396	311	311

Table 8. Selected Calculated and Observed Vibrational Data for Mo_4OXA

band	Mo_4OXA_{obs} ν/cm^{-1}	$Mo_4{}^{13}C$-OXA_{obs} ν/cm^{-1}	Δ_{obs} ν/cm^{-1}	Mo_4OXA_{calc} ν/cm^{-1}	$Mo_4{}^{13}C$-OXA_{calc} ν/cm^{-1}	Δ_{calc} ν/cm^{-1}
ν_1	1411	1367	−44	1423	1380	−43
ν_2	932	927	−5	945	938	−7
ν_3	576	573	−3	584	583	−1

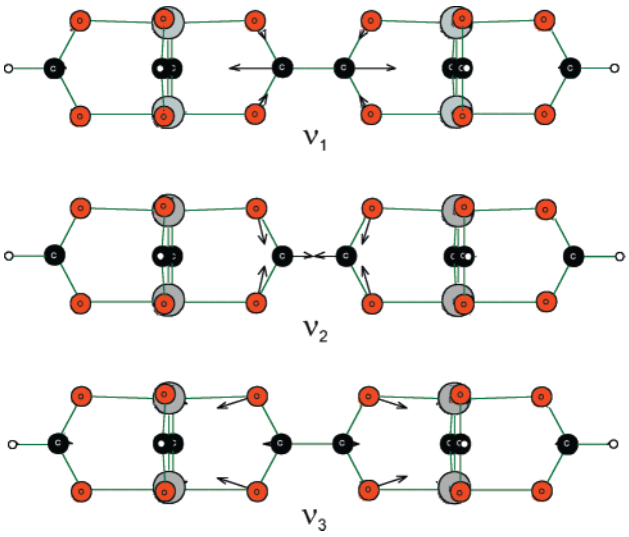

Figure 9. Representations of the calculated $\nu_1(a_{1g})$, $\nu_2(a_{1g})$, and $\nu_3(a_{1g})$ normal modes of D_{2h} $(HCO_2)_3Mo_2(\mu\text{-}O_2CCO_2)Mo_2(O_2CH)_3$.

of the metal atoms, W > Mo > K, and also to back-bonding into the oxalate LUMO, which weakens the C−O bonds and is more extensive for tungsten than for molybdenum.

As a further aid in interpreting the Raman and resonance Raman spectra, vibrational frequency calculations were performed on the optimized D_{2h} model $(HCO_2)_3M_2(\mu\text{-}O_2CCO_2)\text{-}M_2(O_2CH)_3$ complexes using Gaussian 98.[20] Despite the apparent complexity of the systems, for M = Mo, there are three totally symmetric modes, ν_1, ν_2, and ν_3, that are each almost totally localized on the oxalate ligand. The predicted normal modes are depicted as atomic displacements in Figure 9, and the predicted wavenumbers for the ν_1, ν_2, and ν_3 modes of the ^{12}C and ^{13}C oxalate-bridged isotopomers are given in Table 8, along with the experimentally obtained values. The calculated gas-phase values, and their isotopic shifts, are clearly in good agreement with those obtained for the solid state, given the fact that the latter would also be influenced by the intermolecular M−O interactions described earlier.

The atomic displacements qualitatively explain why ν_1 shows greater resonance enhancement than ν_2 or ν_3. The HOMO $^1b_{2g}$ to lowest $^1b_{3u}$ electronic transition takes an electron from an orbital that is predominantly M_4 δ bonding, but weakly C−C antibonding and C−O bonding, to an oxalate-based π orbital that is both C−C π bonding and C−O π antibonding (see Figure 4). The expected shortening of the C−C bond and lengthening of the C−O bonds on electronic excitation is mirrored by the atomic displacements of ν_1. Related calculations for the tungsten model complex give qualitatively similar results for the identities of the ν_1, ν_2, and ν_3 modes.

Electronic Spectra. Given that the Raman data support the previously expressed view that the lowest energy bands in the visible spectra of the M_4OXA complexes are MLCT transitions,[1] and recognizing that the features seen for the W_4OXA compound in the room-temperature solution electronic spectrum in THF appear to be a vibronic progression, we have made a more thorough examination by recording absorption spectra as a function of temperature in 2-MeTHF. The spectra of the complexes have also been obtained as Nujol mulls. Comparisons of the absorption spectra obtained at 300 and 2 K in 2-MeTHF, and the mull spectra at 80 K, are shown for Mo_4OXA and W_4-OXA in Figures 10 and 11, respectively.

Two important observations are immediately apparent from the spectra: (i) The mull spectra are red-shifted with respect to the solution spectra, and furthermore, the spectra recorded at 2 K are red-shifted with respect to those at 300 K. (ii) Vibronic features are apparent at low temperatures for both the mull and glass spectra in each case, and most obviously for W_4OXA. A third observation, although not evident in Figures 10 and 11, is that the spectra recorded as mulls do not show thermochromic shifts.

In the spectra of the 2-MeTHF glasses at 2 K, there appear to be two vibronic progressions, with spacings of ca. 1540 cm^{-1} for W_4OXA and ca. 1490 cm^{-1} for Mo_4OXA. The two progressions are separated by ca. 860 cm^{-1} in the former case and by ca. 670 cm^{-1} in the latter. At 2 K the progressions are near-baseline-resolved for W_4OXA, whereas the Mo_4OXA spectra reveal similar behavior but with poorer resolution.

The influence of temperature on the electronic absorption spectra of the complexes has been studied by recording spectra at 2, 10, 25, 50, 77, 100, 125, 150, 175, 200, 225, 250, 275, 300, and 325 K in 2-MeTHF solution. Selected spectra are shown for W_4OXA in Figure 12. Upon lowering the temperature to 2 K, a smooth bathochromic shift of each component of each progression is observed as the peaks begin to sharpen, with the lowest energy transition shifting by ca. 50 nm, and the intensity of the transition trebling.

The observed vibrational bands, which relate to the photoexcited molecules, M_4OXA^*, would be expected to have significant oxalate character based on our earlier description of

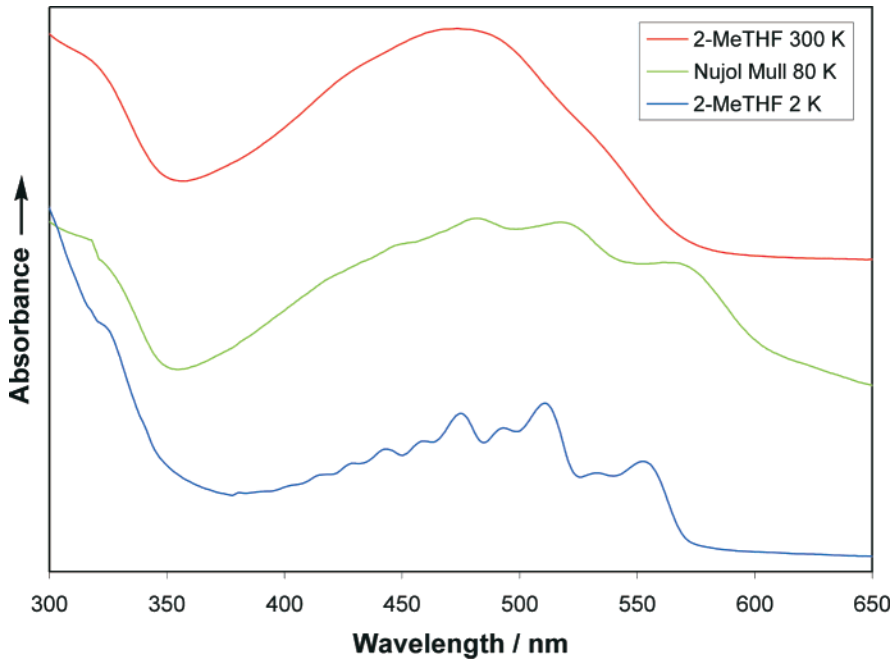

Figure 10. Electronic absorption spectra of Mo_4OXA as a 2-methyltetrahydrofuran solution at 300 K, a Nujol mull at 80 K, and a 2-methyltetrahydrofuran glass at 2 K.

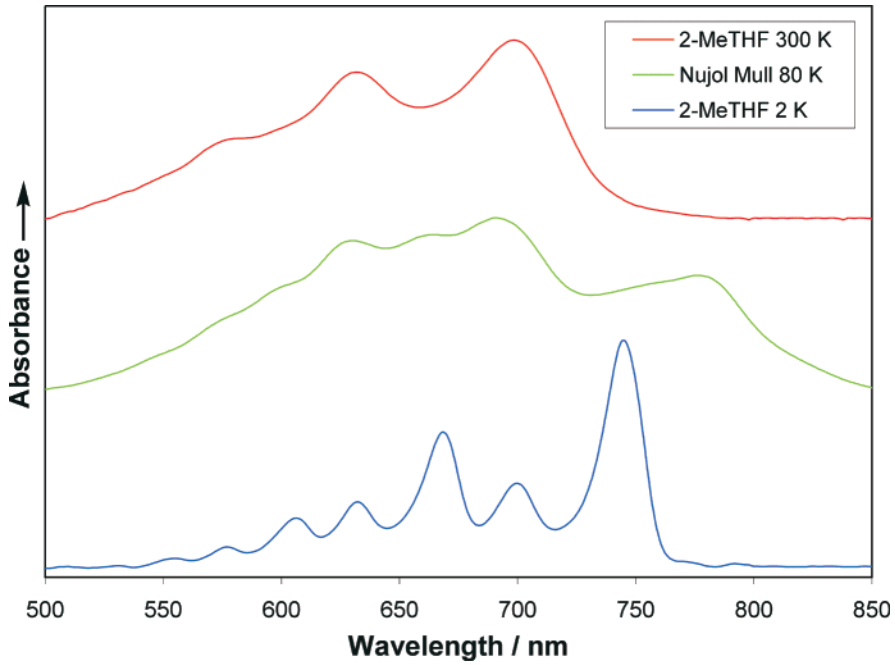

Figure 11. Electronic absorption spectra of W_4OXA as a 2-methyltetrahydrofuran solution at 300 K, a Nujol mull at 80 K, and a 2-methyltetrahydrofuran glass at 2 K.

the lowest vacant b_{3u} oxalate-based orbital and the reported resonance Raman data. To probe this matter further, spectra were also obtained for the μ-$O_2{}^{13}C{}^{13}CO_2$ isotopomers. A comparison of the spectra for the ^{12}C (natural abundance) and ^{13}C (99% abundance) isotopomers of W_4OXA is shown in Figure S6 in the Supporting Information. The wavenumbers of the transition origins are unaffected by isotopic substitution, but the progression intervals are shifted by ca. 50 cm^{-1} on ^{13}C labeling. A summary of the vibronic features in the excited-state complexes, M_4OXA^*, is given in Table 9.

The thermochromic shifts of the electronic transitions in solution are understandable in terms of a preference toward adoption of the more planar structure at lower temperatures. Note that even in the 2-MeTHF glass (below ~140 K), there is significant thermochromism. With decreasing temperature, the molar absorptivity increases dramatically because the absorptivity of this MLCT band is proportional to the square of the overlap of the b_{3u} M_4 δ and oxalate LUMO orbitals, which is at a maximum for $\theta = 0°$. The calculated oscillator strengths for the M_4OXA compounds (Table 2) are in the order W > Mo and are large for the D_{2h} formate model compound.

The emission spectra of M_4OXA have also been examined in 2-MeTHF solution at room temperature. The spectra for W_4-OXA are shown in Figure 13 along with the absorption

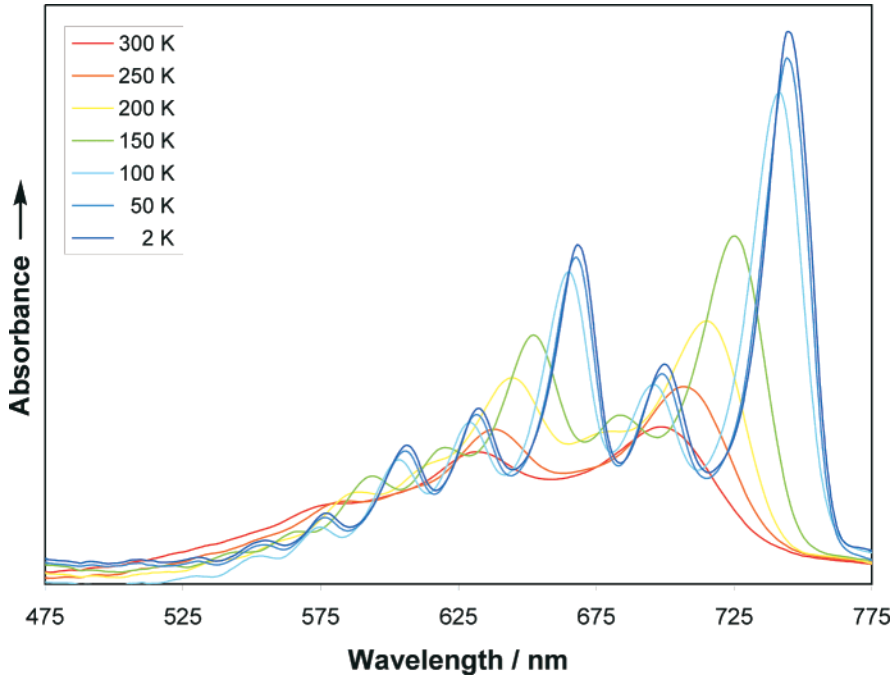

Figure 12. Electronic absorption spectra of W_4OXA at 2, 50, 100, 150, 200, 250, and 300 K in 2-methyltetrahydrofuran solution.

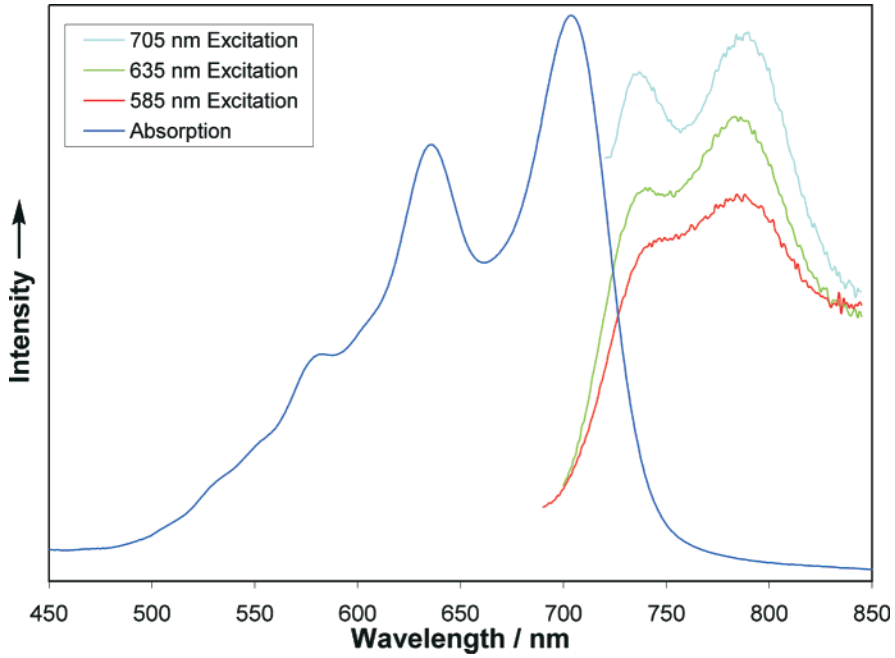

Figure 13. Emission spectra of W_4OXA at room temperature in 2-methyltetrahydrofuran solution, measured using 705, 635, and 585 nm excitation, respectively, along with the electronic spectrum of the complex recorded at room temperature.

Table 9. Summary of the Wavenumbers of the Progression Forming Modes Observed in the Electronic Spectra of Mo_4OXA, W_4OXA, and $W_4{}^{13}$C-OXA[a]

	Mo_4OXA ν/cm^{-1}	W_4OXA ν/cm^{-1}	$W_4{}^{13}$C-OXA ν/cm^{-1}
first origin	18 080	13 420	13 420
second origin	18 080 + 670	13 420 + 860	13 420 + 860
progression interval	1490	1540	1490

[a] As frozen glasses in 2-methyltetrahydrofuran at 2 K.

spectrum, and the spectra for Mo_4OXA are given in Figure S7 in the Supporting Information. There is clearly vibronic structure with an interval of ca. 930 cm^{-1} in the emission spectrum of W_4OXA, though this is not as well resolved as in the absorption spectrum. Estimates of the lifetimes of the emissive states are currently under investigation as well as other spectroscopic investigations of these compounds.

For compounds with M−M quadruple bonds, the assignment of the $\delta \rightarrow \delta^*$ electronic transition has a long and interesting history.[2] At low temperatures, this absorption band often reveals a vibronic progression in ν(M−M) relating to the excited-state molecule. In several instances, other totally symmetric M−L modes are also observed. In the emission spectra, vibronic features have also been observed, and their assignment has not been without considerable discussion, as it is evident that the

excited-state geometry may or may not be closely related to that of the ground-state molecule, and extensive coupling of M−M and M−L vibrational modes can occur.[2]

In our study, it is clear that we are not dealing with M_4 δ-to-δ^* transitions but, instead, with MLCT transitions to the oxalate. The origins of the low-energy absorption and emission bands do not coincide, and the spectra are not mirror images of one another. The M_4OXA and M_4OXA* compounds have different geometries, and, because of the Duschinsky effect, the coupling of the totally symmetric vibrational modes in the excited state is likely to be quite different from that in the ground state. We propose the assignment for the progression based on 1540 (M = W) and 1490 cm^{-1} (M = Mo) in the excited-state M_4OXA* species to be the ν_1 mode localized on the oxalate ligand. Similarly, the origin of the second progression is shifted by 860 (M = W) or 670 cm^{-1} (M = Mo) from the origin of the first progression, which is likely to be ν_2. In the photoexcited state, we expect to find a more planar oxalate unit as a result of populating a C−C π bonding molecular orbital, which is also C−O π antibonding. Populating this orbital leads to ν_1 for the M_4OXA* species having a higher wavenumber than in the ground-state species M_4OXA. The isotopic shift ($^{13}C/^{12}C$) of ca. 50 cm^{-1} seen in ν_1 for W_4OXA* is comparable to that of 43 cm^{-1} observed for ground-state W_4OXA. The isotopic shift of ν_2 for M_4OXA* is insignificant in comparison to that of ν_1, which parallels the trend in the enhancement of the Raman spectra of ground-state M_4OXA.

Concluding Remarks

The use of XRPD has allowed us to establish the nature of the molecular packing in the solid-state structures of the M_4-OXA compounds (M = Mo or W). The techniques we described are likely to gain in utility and popularity as programs become more sophisticated and chemists become more and more interested in molecular design and architectural control of assemblies in the solid state. While the technique is not likely to rival single-crystal X-ray crystallography, particularly with respect to the determination of precise bond distances and angles, it can provide valuable structural information that might otherwise be unavailable in the absence of single crystals.

The Raman, resonance Raman, and variable-temperature electronic spectra of these oxalate-linked "dimers of dimers" reveal the richness of orbital mixing in these extended π systems, both in the ground and excited states. Although much can now be rationalized based on the electronic structure calculations, there clearly remains more to be understood. In particular, the vibrational features that are seen in the electronic absorption spectra at low temperatures pose a challenge. Geometry and electronic structure optimization of species in electronically excited states is currently unfeasible for other than very small model systems, and hence meaningful predictions of the vibrational spectra of such excited state species are not currently possible.

The barrier to rotation about the central oxalate C−C bond in the M_4OXA compounds is clearly very small, as indicated by the DFT calculations and by the thermochromism displayed in solution. In the ground state, the coupling between the $M_2\cdots M_2$ centers is at a maximum for planar oxalate, $\theta = 0$, and a minimum for a twisted (D_{2d}) geometry, $\theta = 90°$. This correlates with the δ orbital splitting which is, furthermore, sensitive to the metal. The energy of the electronic transition M_2 δ to the low-lying vacant oxalate-based orbital also varies greatly with respect to the torsional angle θ. The M_4OXA molecules have several potential modes of binding substrates, as is evident from the solid-state structure. We would therefore expect that their spectroelectrochemical properties will be very solvent dependent and, furthermore, substrate binding perhaps through hydrogen bonding which favors a twisted or a planar oxalate-group will have a most dramatic effect. Such changes could form the basis for signaling and molecular recognition, and investigations of these notions are currently underway.

Experimental Section

Due to the air-sensitive nature of the complexes, all were synthesized and manipulated under dinitrogen or argon atmospheres using either standard Schlenk-line or drybox techniques. The preparation of the M_4-OXA compounds followed previously described procedures.[1] Toluene and hexane were predried over activated molecular sieves and refluxed over molten sodium and potassium, respectively, under an atmosphere of dinitrogen, collected by distillation, and then degassed. ^{13}C-labeled oxalic acid (Cambridge Isotope Laboratories Inc., >99% ^{13}C) was dried and degassed in vacuo at 50 °C prior to use. Samples of the complexes were stored in sealed ampules or capillaries in a dinitrogen-filled drybox. $K_2C_2O_4\cdot H_2O$ (BDH, Analar >99.99%) was used as received. $K_2{}^{13}C_2O_4\cdot H_2O$ was prepared from the reaction between ^{13}C-labeled oxalic acid and potassium bicarbonate.

Solid-State CPMAS NMR Spectroscopy. Solid-state cross polarization, magic angle spinning[40,41] (CPMAS) NMR spectra were obtained on a Bruker DMX400 NMR spectrometer operating at a ^1H frequency of 400.14 MHz and a ^{13}C frequency of 100.64 MHz utilizing a 4 mm high-power CPMAS probe, on samples of the ground compound sealed in a glass spinner insert. Spectra were acquired with ramped cross polarization[42,43] and high-power two-pulse phase-modulated (TPPM) decoupling.[44] CP contact times were 5 ms, the decoupling field strengths were approximately 80 kHz, the recycle delay was 2 s, and the sample spinning frequency was 10 kHz. A total of 1K of complex data with a dwell time of 33.2 μs (spectral width of 30 kHz or 300 ppm) were zero filled to 8K of complex data points, exponentially apodized with a 5 Hz line broadening, and Fourier transformed to produce the NMR spectra, which were then referenced to the carbonyl resonance of solid glycine at 176.03 ppm with respect to TMS. ^{13}C NMR data for Mo_4-OXA (solid, 100.64 MHz, 298 K): δ (ppm) 190.8 (cis and trans $O_2CC(CH_3)_3$), 156.9 (μ-O_2CCO_2), 40.9 (cis $O_2CC(CH_3)_3$), 40.1 (trans $O_2CC(CH_3)_3$), 29.8 29.4 28.7 (cis and trans $O_2CC(CH_3)_3$).

Powder X-ray Diffraction and Structure Solution. Powder samples of M_4OXA were ground using a pestle and mortar and then packed and sealed in 0.7 mm diameter glass capillaries (W. Müller). X-ray powder diffraction patterns were collected either at the Brookhaven National Laboratory or in-house. At Brookhaven, the data were collected at the X7A beamline, rotating the capillaries at 1−2 Hz. Monochromatic radiation with a wavelength of 0.8000 Å was obtained using a channel-cut double-crystal Si(111) monochromator. The data were collected by step scanning over the angular range $4° < 2\theta < 30°$ using a linear position-sensitive detector (PSD). In-house, data were collected using a Bruker D8 diffractometer equipped with copper radiation and an incident beam Ge(111) monochromator. Again the capillaries were

(40) Pines, A.; Gibby, M. G.; Waugh, J. S. *J. Chem. Phys.* **1973**, *59*, 569−590.
(41) Stejskal, E. O.; Schaefer, J.; Waugh, J. S. *J. Magn. Reson.* **1977**, *28*, 105−112.
(42) Hediger, S.; Meier, B. H.; Kurur, N. D.; Bodenhausen, G.; Ernst, R. R. *Chem. Phys. Lett.* **1994**, *223*, 283−288.
(43) Metz, G.; Wu, X.; Smith, S. O. *J. Magn. Reson., Ser. A* **1994**, *110*, 219−227.
(44) Bennett, A. E.; Rienstra, C. M.; Auger, M.; Lakshmi, K. V.; Griffin, R. G. *J. Chem. Phys.* **1995**, *103*, 6951−6958.

rotated during data collection, and a scintillation counter was used as the detector while step scanning over the angular range $3° < 2\theta < 22°$.

Molecular and Electronic Structure Calculations. Molecular and electronic structure determinations on the models $(HCO_2)_3M_2(\mu\text{-}O_2CCO_2)M_2(O_2CH)_3$ were performed with density functional theory (DFT) using both the Gaussian 98[20] and ADF 2000.01[21−24] programs. With Gaussian 98, we have used the B3LYP[45−47] functional along with the 6-31G* basis set for H, C and O,[48] and the SDD energy-consistent pseudopotentials for Mo and W.[49] With ADF 2000, we have used the exchange and correlation functionals of Perdew and Wang,[50,51] along with a double-ζ Slater basis set with d-type polarization functions, for H, C, and O (1s frozen core for C and O), and triple-ζ basis sets were employed for both Mo (3d frozen core) and W (4d frozen core). ZORA scalar relativistic corrections were applied to both Mo and W systems under ADF.[52−56] All geometries were fully optimized at the above levels using the default optimization criterion of the respective programs. Orbital analyses were completed with GaussView.[57] Electronic absorption spectra were predicted using the TDDFT method implemented within the Gaussian 98 and ADF 2000.01 programs and using the default optimization criteria.[30−34]

Raman and Resonance Raman Spectra. Spectra were recorded on a Spex 1401 spectrometer following excitation with a range of different lines from Coherent Innova 70 Ar^+ and 301 Kr^+ lasers. Wavenumber calibration was achieved by superimposing neon emission lines onto the Raman spectra, resulting in an accuracy of ± 1 cm^{-1}. For Mo_4OXA and $Mo_2(O_2C^tBu)_4$, disks of ca. 50% sample in either KCl or K_2SO_4 were prepared. The spectra were recorded with the sample disks held at liquid nitrogen temperature (ca. 80 K) in a purpose-built cryostat. For W_4OXA and $W_2(O_2C^tBu)_4$, the capillary tubes were mounted on the tip of the cryostat without further preparation.

Variable-Temperature Electronic Absorption Spectra. Spectra were obtained in the temperature range 2−325 K using an Oxford Instruments OptistatBath helium cryostat placed within the sample compartment of a Perkin-Elmer Lambda 19 UV−vis−NIR absorption spectrometer. Samples were prepared in an inert atmosphere drybox and injected into a 150 μL copper cell consisting of two quartz windows separated by a permeable synthetic rubber spacer. Spectra of the compounds in the solution state were obtained in thoroughly degassed optical quality anhydrous 2-methyltetrahydrofuran (2-MeTHF, Aldrich), which forms a glass at ca. 130−40 K, while spectra of the compounds in the solid state were obtained as Nujol (Wilmad) mulls. All spectra were cumulatively averaged from two or three scans taken with a scan rate of 120 nm min^{-1} and using a 1−2 nm band-pass.

Emission Spectra. Spectra were recorded in the solution state in thoroughly degassed optical quality anhydrous 2-methyltetrahydrofuran (2-MeTHF, Aldrich) using a SPEX FluoroMax-2 spectrometer equipped with a 150 W xenon source, a red-sensitive R928P photomultiplier tube, and DataMax-Std software. All spectra were cumulatively averaged from three scans taken with a scan rate of 60 nm min^{-1}.

Acknowledgment. We thank the National Science Foundation at Indiana University and The Ohio State University, the Engineering and Physical Sciences Research Council, and the University of London Intercollegiate Research Service for financial support. The Ohio Supercomputer Center is gratefully acknowledged for computational resources with which the DFT calculations were performed. The Campus Chemical Instrumentation Center is also gratefully acknowledged for use of NMR facilities.

Supporting Information Available: X-ray powder diffraction analysis and Raman data (PDF). This material is available free of charge via the Internet at http://pubs.acs.org.

JA011786J

(45) Becke, A. D. *Phys. Rev. A: Gen. Phys.* **1988**, *38*, 3098−3100.
(46) Becke, A. D. *J. Chem. Phys.* **1993**, *98*, 5648−5652.
(47) Lee, C.; Yang, W.; Parr, R. G. *Phys. Rev. B: Condens. Matter* **1988**, *37*, 785−789.
(48) Hehre, W. J.; Radom, L.; Schleyer, P. v. R.; Pople, J. A. *Ab initio Molecular Orbital Theory*; John Wiley & Sons: New York, 1986.
(49) Andrae, D.; Haeussermann, U.; Dolg, M.; Stoll, H.; Preuss, H. *Theor. Chim. Acta* **1990**, *77*, 123−141.
(50) Perdew, J. P.; Wang, Y. *Phys. Rev. B: Condens. Matter* **1992**, *45*, 13244.
(51) Perdew, J. P.; Chevary, J. A.; Vosko, S. H.; Jackson, K. A.; Pederson, M. R.; Singh, D. J.; Fiolhais, C. *Phys. Rev. B: Condens. Matter* **1992**, *46*, 6671−6687.
(52) van Lenthe, E.; Baerends, E. J.; Snijders, J. G. *J. Chem. Phys.* **1993**, *99*, 4597−4610.
(53) van Lenthe, E.; Baerends, E. J.; Snijders, J. G. *J. Chem. Phys.* **1994**, *101*, 9783−9792.
(54) van Lenthe, E.; Snijders, J. G.; Baerends, E. J. *J. Chem. Phys.* **1996**, *105*, 6505−6516.
(55) van Lenthe, E.; Van Leeuwen, R.; Baerends, E. J.; Snijders, J. G. *Int. J. Quantum Chem.* **1996**, *57*, 281−293.
(56) van Lenthe, E.; Ehlers, A.; Baerends, E. J. *J. Chem. Phys.* **1999**, *110*, 8943−8953.
(57) *GaussView 2.1*; Gaussian Inc.: Pittsburgh, PA, 1998.